sensors

MDPI

Article

First-Order Linear Mechatronics Model for Closed-Loop MEMS Disk Resonator Gyroscope

Hao Wang, Xiupu Wang and Jianbing Xie *

MOE Key Laboratory of Micro and Nano Systems for Aerospace, Northwestern Polytechnical University, Xi'an 710072, China; wangh@mail.nwpu.edu.cn (H.W.); wang_xp@mail.nwpu.edu.cn (X.W.)

* Correspondence: xiejb@nwpu.edu.cn

Received: 22 September 2020; Accepted: 9 November 2020; Published: 12 November 2020

Abstract: In this paper, a first-order closed-loop mechatronics model of a micro-electromechanical system (MEMS) disk resonator gyroscope (DRG) with a configurable ASIC is established for closed-loop design and performance analysis. There are usually some nonlinear modules in the gyroscope mechatronics model, and it is difficult to design the closed-loop controllers using classical automatic control theory. An order-reduction method (ORM) based on the Laplace transform and inverse Laplace transform is proposed to linearize the nonlinear modules. The linearized model is proved to show good agreement with the original mechatronics model in terms of system response. The experimental verification was conducted to demonstrate the validation of this method.

Keywords: MEMS; mechatronics model; order-reduction method (ORM); disk resonator gyroscope (DRG)

1. Introduction

The micro-electromechanical system (MEMS) disk resonator gyroscope (DRG) is a typical wine-glass mode gyroscope and it has become more favorable for high performance MEMS gyroscopes [1–4]. A lot of progress has been made on the disk resonator and DRG, including Q factor optimization [5–8], frequency tuning [9–11], resonator noise analysis and structure optimization [12–15], microcosmic dynamics analysis [16,17], nonlinear models of disk resonators [18,19], and fabrication processes [20,21].

Mostly, researchers are more concerned with accuracy or bias stability. Factors like bandwidth and closed-loop scale factor are usually ignored. The influence of closed-loop system and controller on detection bandwidth, settling time, and closed-loop gain, has not been discussed so far. For example, it is well believed that the bandwidth of a tuning-fork gyroscope is determined by the frequency difference of primary mode and secondary mode. For a central symmetrical gyroscope like DRG, however, the frequency difference is close to 0 after tuning, and the factors or the design method affecting the bandwidth have not been studied. Thus, it is of great significance to study how to determine these systematic parameters. These factors of a closed-loop gyroscopic system, such as bandwidth, closed-loop scale factor, settling time, could be determined by the classical automatic control theory. In an original closed-loop MEMS gyroscope system, there are typically some nonlinear modules, such as the modulator, demodulator, oscillator, and phase detector, making it difficult to design closed-loop controllers and analyze performance terms using classical automatic control theory. Therefore, it is quite necessary to linearize the mechatronics models in order to facilitate the closed-loop design [22–27].

In our previous work, we tried to model a vibrating ring gyroscope (VRG) [28]; however, it is mainly based on the force rebalance loop. In this paper, a mechatronics model is established for a MEMS disk resonator gyroscope (DRG) with a configurable ASIC (Application Specific Integrated Circuit).

A model order-reduction method (ORM) based on Laplace transform and inverse Laplace transform is proposed to linearize the mechatronics model. Therefore, the gyroscopic model with a modulator and a demodulator in the AGC loop and rebalance loop is linearized to a first-order model, and the gyroscopic model with an oscillator and a phase detector in PLL is also linearized to a gain term. With the order-reduction model, the closed-loop controller and systematic terms can be easily designed using automatic control theory.

2. MEMS DRG and the Configurable ASIC

2.1. MEMS Disk Resonator

MEMS DRG is a typical wineglass mode resonator. A simplified model of a resonant vibratory gyroscope including equivalent noise force terms is given by [29]

$$\begin{aligned} m_x\frac{d^2x}{dt^2} + c_x\frac{dx}{dt} + k_x x &= F_{elec} + 2m_y\Omega_z\frac{dy}{dt} + F_{noise,x}(c_x,t) \\ m_y\frac{d^2y}{dt^2} + c_y\frac{dy}{dt} + k_y y &= -2m_x\Omega_z\frac{dx}{dt} + F_{noise,y}(c_y,t) \end{aligned} \tag{1}$$

where x, m_x, c_x, and k_x are the vibration displacement, effective mass, damping coefficient, and stiffness of the primary mode, respectively, and y, m_y, c_y, and k_y are the vibration displacement, effective mass, damping coefficient, and stiffness of the secondary mode, respectively. Ω_z is the angular rate of Z-axis. $F_{noise,x}$ and $F_{noise,y}$ are mechanical noise of the primary mode and the secondary mode, respectively.

Ideally, it is assumed that the MEMS DRG is perfectly fabricated and the resonant frequencies, effective masses, and damping coefficient of the two modes are equal, i.e., $m_x = m_y = m_0$, $k_x = k_y = k$, $c_x = c_y = c$. Then, the transfer functions of the two modes can both be expressed by

$$G(s) = \frac{1}{m_0 s^2 + cs + k} = \frac{\frac{1}{m}}{s^2 + 2\zeta\omega_n s + \omega_n^2}, \tag{2}$$

where ω_n is the resonant frequency, ζ is the damping ratio, and $\zeta = \frac{c}{\sqrt{km_0}}$.

The DRG in this paper performs as n = 2 mode, as shown in Figure 1, and it enables differential driving and differential sensing. The diagrammatic sketch of the MEMS disk resonator and its electrodes involved in this paper is shown in Figure 1. The frequency split of the two modes can be tuned by the frequency tuning electrodes. The detailed parameters regarding DRG which will be used in later calculations are shown in Table 1.

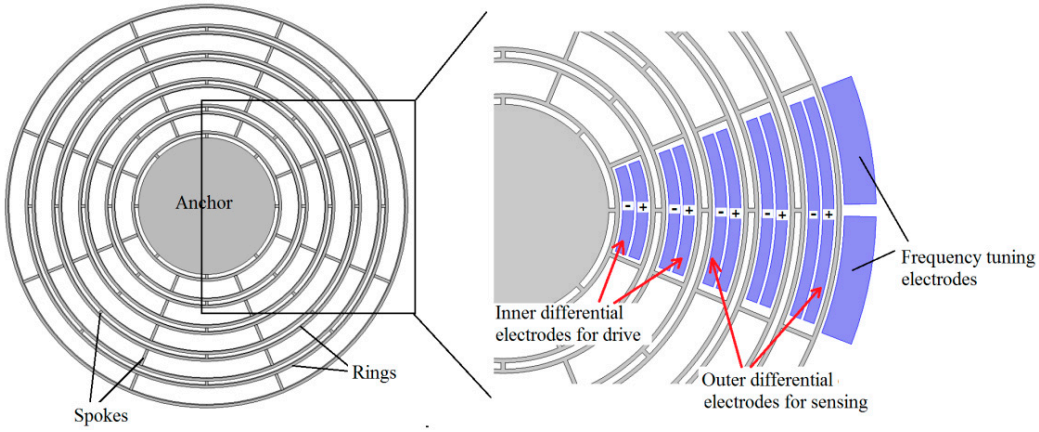

Figure 1. Diagrammatic sketch of MEMS disk resonator.

Table 1. Key parameters of disk resonator and its sensing system.

Parameter	Value
Effective mass/m	1.67×10^{-6} kg
Q factor/Q	13,000
Resonant frequency/f_0	12,343.3 Hz
Angular gain/A_g	0.393
Sense capacitance/C_0	7.6 pF
Drive capacitance/C_{drive}	3.4 pF
Electrodes' spacing/x_0	5 µm
Primary amplitude/A_x	0.5 µm
Feedback capacitance of CV/C_f	10 pF
DC bias voltage/V_{bias}	10 V

2.2. A Configurable Closed-Loop ASIC for MEMS DRG

The closed-loop ASIC is an important device in achieving close-loop control. A configurable ASIC for MEMS gyroscopes is employed in this paper. The functions of the ASIC include providing high-voltage DC bias, temperature sensing and compensation, and frequency split tuning. However, the most important function is to realize closed-loop control for the MEMS gyroscope.

The architecture of the DRG closed-loop system is shown in Figure 2. The blue parts in the loops are configurable modules, which can be altered for performance terms design.

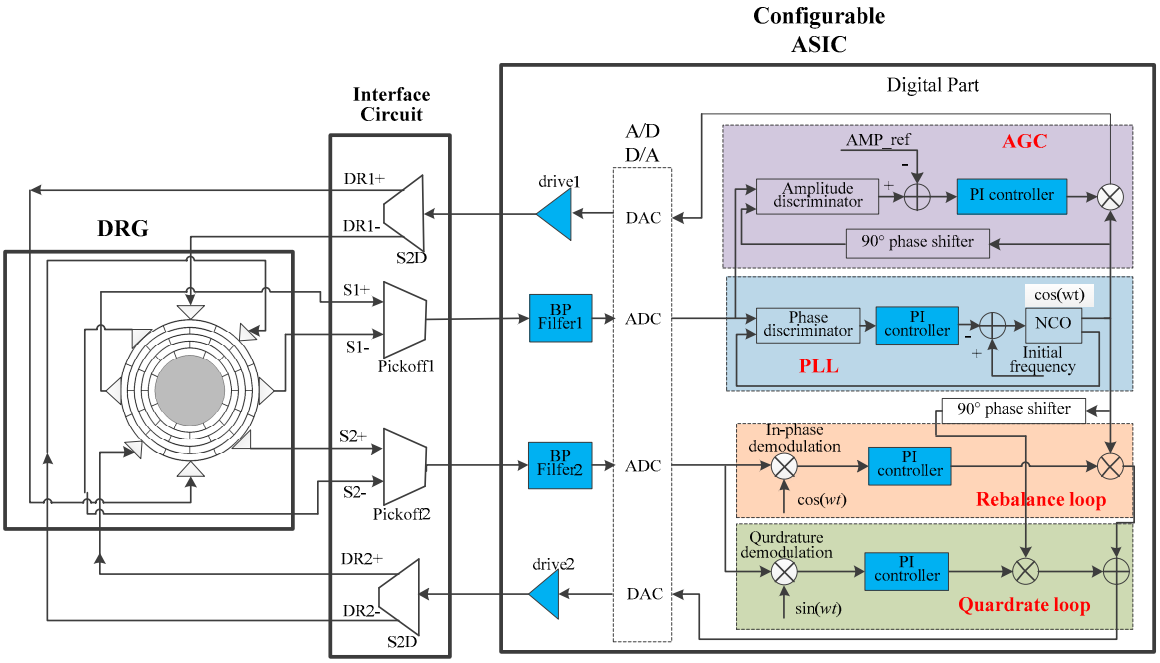

Figure 2. Closed-loop system constituted by the MEMS disk resonator and a configurable ASIC.

The analog parts of the ASIC mainly include analog band-pass filters, analog to digital converters (ADCs), digital to analog converters (DACs), and drive circuits. The digital parts of the ASIC can realize functions such as signal demodulation, signal modulation, PI controllers, and numerically controlled oscillator (NCO).

An interface circuit is needed between the resonator and ASIC. The interface circuit picks off the differential displacement signals and converts them to a single-end signal, and converts the single-end drive signal to differential drive signals.

An original mechatronic model is established on the Simulink platform as shown in Figure 3, which is consistent with the actual system consisting of the circuits and resonator.

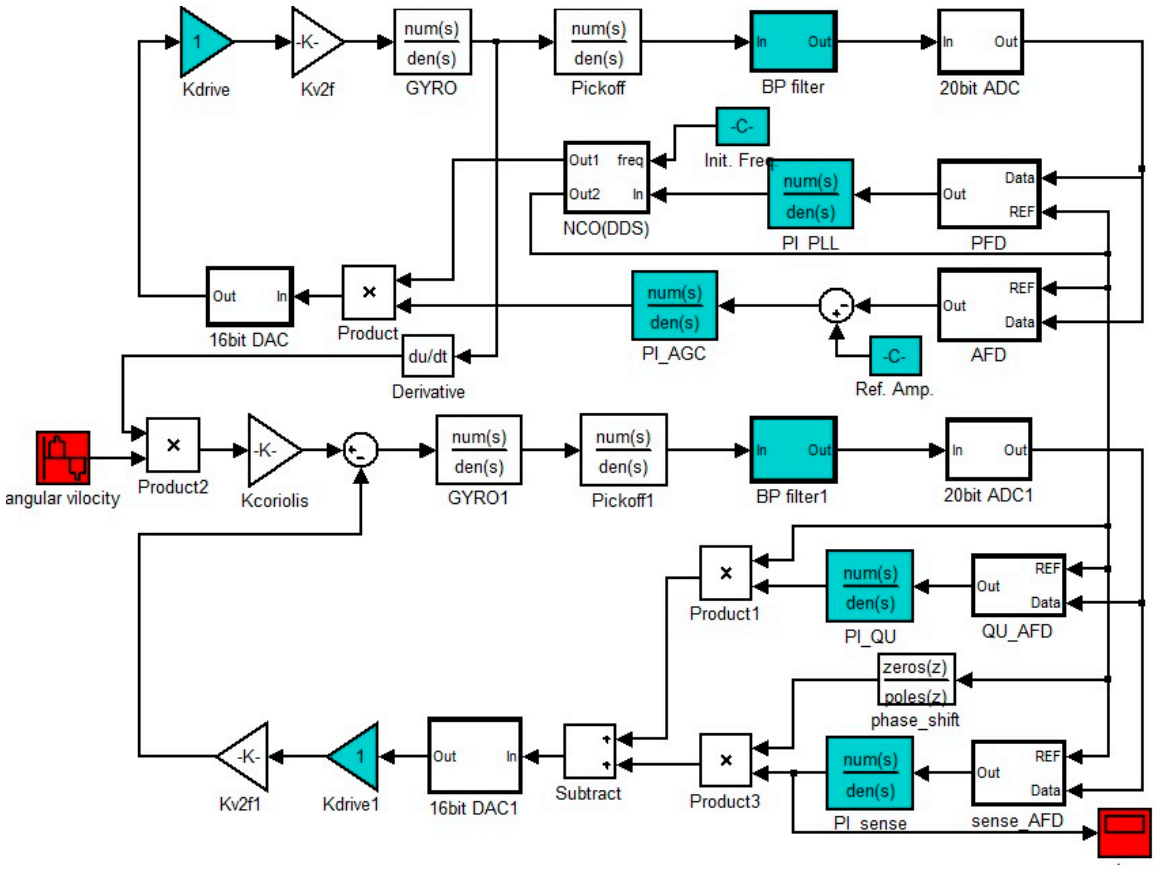

Figure 3. Original mechatronics model for DRG with a configurable ASIC.

The main modules involved in the model are introduced as follows.

(1) Pickoff circuit

The pickoff circuits mainly implement *C*/*V* (capacitance to voltage) detection. The *C*/*V* circuit employs a charge amplifier and its basic principle is shown in Figure 4.

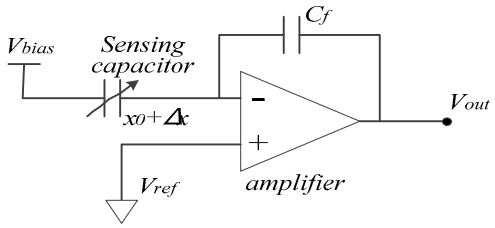

Figure 4. *C*/*V* circuit implemented by a charge amplifier.

The gain of the *C*/*V* circuit k_{CV}, which represents the gain from displacement x to output voltage V_{out}, is

$$k_{CV} = \frac{\partial V_{out}}{\partial x} = \frac{V_{bias} C_0}{x_0 C_f}, \tag{3}$$

where C_0 is the sensing capacitance, V_{bias} is the DC bias voltage forced on proof mass, x_0 is the spacing of electrodes' gaps, and C_f is the feedback capacitance.

(2) Analog band-pass filterPickoff circuit

The analog band-pass filter is implemented by a switched capacitor circuit, which mainly filters the white noise and 1/f noise from previous stage circuits. The transfer function of the

band-pass filter is represented by $H_{BPF}(s)$. When the gyroscope resonator vibrates near the resonant frequency, the band-pass filter can be seen as a gain term for the effective signal, denoted by k_{BPF}. The analog band-pass filter is a configurable part whose center frequency and gain can be configured to accommodate different resonators.

(3) ADCs and DACs

The ASIC employs 20-bit sigma-delta ADCs and 16-bit sigma-delta DACs. The gain of ADC is expressed by k_{ADC} and the gain of DAC is expressed by k_{DAC}.

(4) Drive circuit

The drive circuit provides the drive capability for DRG. The gain of drive circuit is configurable, and it is expressed by k_{drive}.

(5) Digital circuit

The digital circuit undertakes the main operations of the closed-loop control system. For the primary mode, the main functions of the digital circuit include digital phase detection, digital demodulation, digital PI controllers, NCO, etc. For the secondary mode, the main operations of the digital circuit include orthogonal demodulation, in-phase demodulation, PI controllers, modulation (digital multiplier), etc.

(6) Gain of electrostatic feedback force

A high DC bias voltage V_{bias} is applied on the mass and the feedback drive voltage V_{drive} is applied on drive electrodes. Thus, the electrostatic feedback force F_{elec} is expressed by

$$F_{\text{elec}} = \frac{1}{2} \times \frac{V_{bias} C_{drive} V_{drive}}{x_0}. \tag{4}$$

Additionally, the gain of the electrostatic feedback force k_{V2F} is

$$k_{V2F} = \frac{1}{2} \times \frac{V_{bias} C_{drive}}{x_0}, \tag{5}$$

where C_{drive} is the drive capacitance.

(7) Gain of Coriolis force

According to the Coriolis Effect [30], the Coriolis force is

$$F_{coriolis} = -4A_g m_0 v_x \times \Omega, \tag{6}$$

where Ag is angular gain, v_x is vibrating velocity of the primary mode, and

$$v_x = \frac{d(A_x \sin(\omega_0 t))}{dt} = A_x \omega_0 \times \cos(\omega_0 t), \tag{7}$$

where $cos(\omega_0 t)$ acts as a modulation term and A_x is amplitude of the primary mode. Thus, the Coriolis gain is

$$k_{coriolis} = -4A_g m_0 A_x \omega_0. \tag{8}$$

The specifications of ASIC and controller are presented in Table 2.

Table 2. Key parameters of disk resonator.

Key Parts of ASIC	Specification	Value
Pickoff circuit/CV	To pickoff the displacement of resonator	$k_{CV} = \frac{\partial V_{out}}{\partial x} = \frac{V_{bias} C_0}{x_0 C_f}$
DAC/ADC	20-bit sigma-delta ADCs and 16-bit sigma-delta DACs	$k_{ADC} = 2^{20}, k_{DAC} = 2^{-16}$
Band-pass filter	The central frequency is configurable	$H_{BPF}(s) = \frac{3.3\times10^5 s}{s^2+4.01s+5.42\times10^9}$
Drive circuit	To provide the drive capability for DRG	Gain is configurable
Electrostatic feedback force	-	$k_{V2F} = \frac{1}{2} \times \frac{V_{bias} C_{drive}}{x_0}$
Gain of Coriolis force	-	$k_{coriolis} = -4A_g m_0 A_x \omega_0$
PI controller	Implemented in an embedded MCU and is configurable	$PI(s) = \frac{b(s+\zeta\omega_n)}{s(s+a)}$, configurable

3. Model Linearizing and PI Controllers' Design for Primary Mode

3.1. AGC Loop Model Order-Reduction and Closed-Loop Design

The AGC loop has frequency-shifting modules, including a modulator and a demodulator, which make the design of a closed-loop system complicated. To design a closed-loop control system using classical automatic control theory, it is necessary to simplify the closed-loop system to obtain a linear system. For this purpose, the order-reduction method (ORM) is proposed in this paper. With the ORM, the system response of a complex high-order system composed of multiple nonlinear modules and a gyroscopic module in series can be derived. The complex high-order system in series can be replaced by a low-order linear system whose system response is equivalent or approximate to the complex high-order system to achieve a linearizing system.

First, the modules that do not change the frequency of effective signals are replaced by gain terms as shown in Figure 5a. This is called the "equivalent gain method". Then, the gain terms are merged as K_1 and K_2, and $K_1 = k_{DAC} \times k_{drive1} \times k_{V2F}$, $K_2 = k_{pickoff} \times k_{BPF} \times k_{ADC}$. The locations of some gain terms are exchanged because this does not change the closed-loop characteristics, as shown in Figure 5b. The term *Amp_ref* is the amplitude control term of primary mode in the digital circuit.

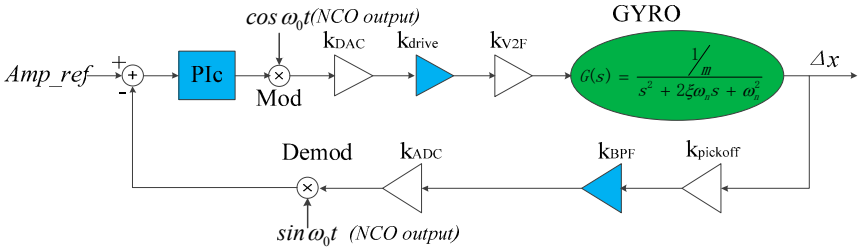

(**a**) Closed-loop AGC with some function parts replaced by gain terms.

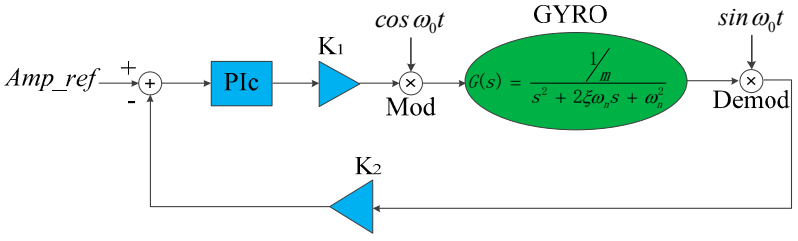

(**b**) Closed-loop AGC with gain terms merged and locations exchanged.

Figure 5. Simplification process of closed-loop AGC.

Second, the controlled objects of the closed-loop are the modules <modulator–gyroscope–demodulator> in series instead of gyroscope according to Figure 5b, thus, the ORM is adopted and the modules <modulator–gyroscope–demodulator> in series are derived as a first-order transfer function $G_1(s)$:

$$G_1(s) = \frac{\frac{1}{2m\omega_n}}{s + \zeta\omega_n}. \tag{9}$$

The derivation process for Equation (9) is given below.

The signal representations of the different nodes are given in Figure 6. The input signal at point A is set to be the unit step signal $\varepsilon(t)$. Then, the signal at point B equals the unit step signal multiplied by the modulation signal $cos(\omega_n t)$, i.e.,

$$Y_B(t) = \varepsilon(t) \times \cos \omega_n t. \tag{10}$$

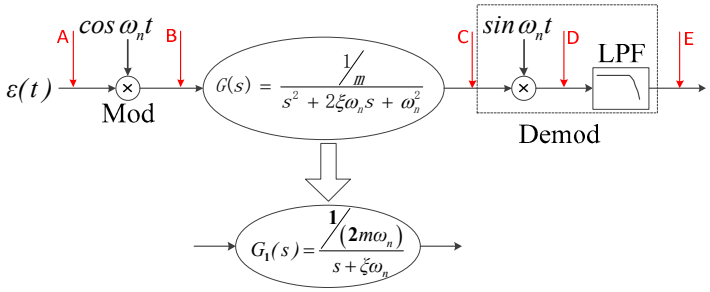

Figure 6. The modules <modulator–gyroscope–demodulator> in series and their equivalent first-order transfer function.

A Laplace transformation is performed on $Y_B(t)$:

$$H_B(s) = L(Y_B(t)) = \frac{s}{s^2 + \omega_n^2}. \tag{11}$$

After the signal passes through the gyroscopic second-order system and reaches point C, the transfer function from point A to point C is

$$\begin{aligned} H_C(s) &= H_B(s) \times G(s) \\ &= \frac{1}{2\zeta\omega_n^2 m} \times [\frac{\omega_n}{s^2+\omega_n^2} - \frac{\omega_n}{s^2+2\zeta\omega_n s+\omega_n^2}] \end{aligned} \tag{12}$$

An inverse Laplace transformation is performed on $H_C(s)$ to obtain a time domain signal at point C:

$$\begin{aligned} Y_C(t) &= L^{-1}(H_C(s)) \\ &= \frac{1}{2\zeta\omega_n^2 m} \times [\sin \omega_n t - \frac{1}{\sqrt{1-\zeta^2}} e^{-\zeta\omega_n t} \sin(\omega_n \sqrt{1-\zeta^2} t)] \end{aligned} \tag{13}$$

For vacuum encapsulation gyroscopes, the Q factor is usually very large and $Q > 10,000$, so $\zeta = \frac{1}{2Q} \to 0$ and $\sqrt{1-\zeta^2} \approx 1$. Then:

$$Y_C(t) = \frac{\sin \omega_n t}{2\zeta\omega_n^2 m} \times (1 - e^{-\zeta\omega_n t}). \tag{14}$$

In the demodulation phase, the signal at point C is multiplied by the demodulation signal $sin(\omega_n t)$ to obtain a signal at point D:

$$\begin{aligned} Y_D(t) &= Y_C(t) \times \sin \omega_n t \\ &= \frac{1}{2\zeta\omega_n^2 m} \times (1 - e^{-\zeta\omega_n t}) \times \tfrac{1}{2}(1 - \cos 2\omega_n t) \end{aligned} \tag{15}$$

The signal at point *D* passes through a low-pass filter in the demodulation module and reaches point *E*, and the high-frequency component $\omega = 2\omega_n$ is filtered out so that only the signal envelope is obtained:

$$Y_E(t) = \frac{1}{2\zeta\omega_n^2 m} \times (1 - e^{-\zeta\omega_n t}). \tag{16}$$

$Y_E(t)$ is the signal that the unit step signal transmits from point *A* to point *E*; that is, $Y_E(t)$ is the unit step response of the modules <modulator–gyroscope–demodulator> in series.

An inverse Laplace transformation is performed on $Y_E(t)$:

$$H_E(s) = L^{-1}(Y_E(t)) = \frac{1}{2\omega_n m} \times (\frac{1}{s(s+\zeta\omega_n)}). \tag{17}$$

It is assumed that the equivalent transfer function of the modules <modulator–gyroscope–demodulator> in series is $G_1(s)$ and

$$G_1(s) = \frac{H_E(s)}{R(s)}, \tag{18}$$

where $R(s)$ is the Laplace transformation of the step signal $\varepsilon(t)$ and $R(s) = L(\varepsilon(t)) = \frac{1}{s}$. Thus:

$$G_1(s) = \frac{\frac{1}{2m\omega_n}}{s + \zeta\omega_n}. \tag{19}$$

Then the AGC loop is linearized to the model shown in Figure 7. After model order-reduction, the closed-loop transfer function of the AGC loop can be expressed by

$$C_{AGC}(s) = \frac{K_1 \times PI(s) \times G_1(s)}{K_1 \times PI(s) \times G_1(s) \times K_2 + 1}. \tag{20}$$

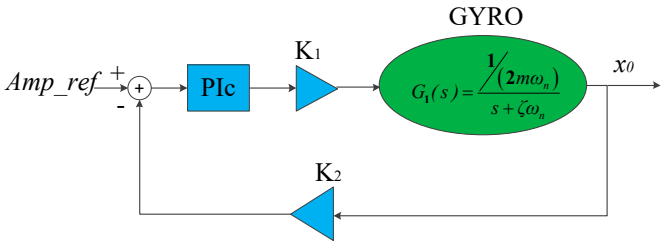

Figure 7. Order-reduction model for AGC loop.

Here, $PI(s)$ represents the transfer function of the PI controller. It is convenient to design the PI controller based on Equation (20). A controller design method based on time domain characteristics is adopted. The structure of the PI controller is

$$PI(s) = \frac{b(s + \zeta\omega_n)}{s(s + a)}. \tag{21}$$

where the terms a and b are the parameters of the PI controller.

Thus, the closed-loop transfer function can be expressed by

$$C_{AGC}(s) = \frac{\frac{\omega_{nc}^2}{K_2}}{s^2 + 2\zeta_c\omega_{nc}s + \omega_{nc}^2} = \frac{K_1 \times \frac{b}{m\omega_n}}{s^2 + as + K_1 \times K_2 \times \frac{b}{m\omega_n}}, \tag{22}$$

where the terms ζ_c and ω_{nc} are the damping ratio and resonant frequency, respectively, of the second-order closed-loop system $C_{AGC}(s)$ and, $2\zeta_c\omega_{nc} = a$, $\omega_{nc} = \sqrt{K_1 \times K_2 \times \frac{b}{m\omega_n}}$.

To avoid overshoot of the system, the systematic damping ratio ζ_c is set to 1; that is, the AGC closed-loop system is a critical damping system. The term $\zeta_c * \omega_{nc}$ determines the systematic bandwidth and the rise time of step response. According to the automatic control theory [31], when $\zeta_c = 1$, the bandwidth Bw is $Bw = 0.64\omega_{nc}$ (rad/s) and the rise time of step response is $Tr = \frac{5.84}{\omega_{nc}}(s)$.

According to the configuring of ASIC and parameters of DRG, $K_1 = 1.36 \times 10^{-9}$ and $K_2 = 3.78 \times 10^{11}$.

When the system bandwidth of the AGC loop is set to 10 Hz, the rise time is 0.06 s, and the PI controller is $PI(s) = \frac{5.432 \times (s+3.232)}{s(s+200)}$; therefore, the closed-loop transfer function is $C(s) = \frac{2.6455 \times 10^{-8}}{s^2+200s+1 \times 10^4}$. When the digital amplitude control term Amp_ref is set to a constant, the amplitude of primary mode A_x is

$$\frac{A_x}{Amp\_ref} = C(s)\Big|_{j\omega=0} = \frac{1}{K_2}, \tag{23}$$

The amplitude of primary mode is set to 0.5 μm; therefore, $Amp\_ref = 1.89 \times 10^5$. The PI controller is introduced to the original model and the linearized model, respectively. The step response of the original model is shown in Figure 8a and the step response of the linearized model is shown in Figure 8b.

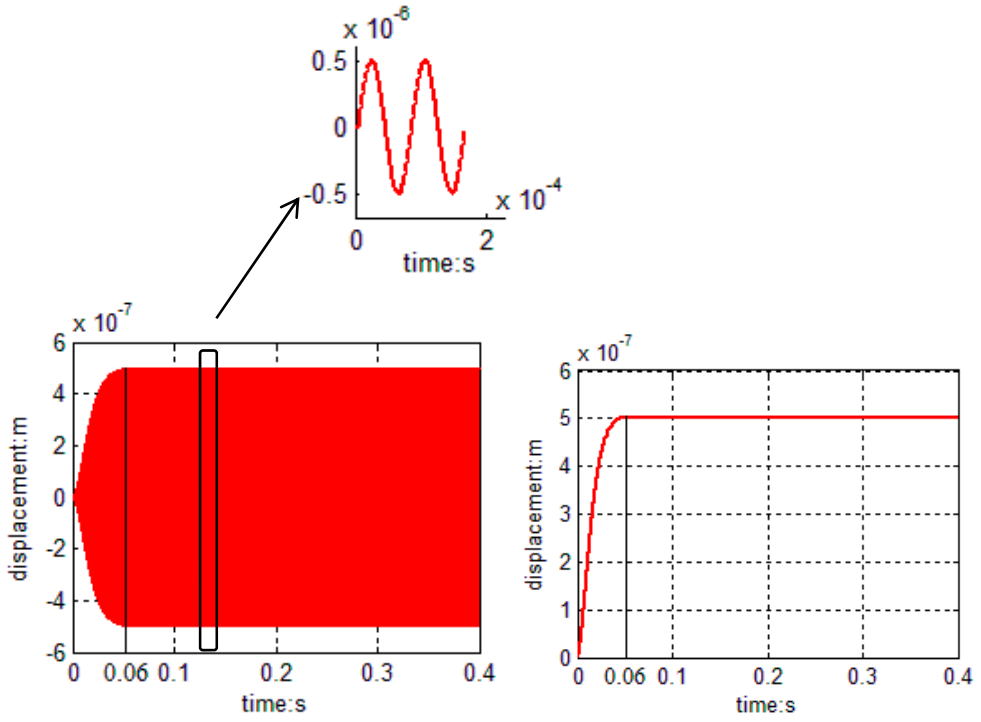

(**a**) (**b**)

Figure 8. (**a**) Step response of AGC original model and (**b**) step response of the AGC linearized model.

According to Figure 8, the rise times of both models are 0.06 s, which are subordinated to designed values, and there is no overshot in both models. The simulation results show that the step response of the linearized model is completely consistent with the envelope of the original model's step response.

The frequency response characteristics are also simulated based on both the linearized model and the original model as shown in Figure 9. The amplitude of the gyroscope in order-reduction model is 5×10^{-7} m while amplitude in original model is 5.07×10^{-7} m. The amplitude error is 1.4%

between the two models. Additionally, 3dB bandwidths of the two models are both 10 Hz, which are quite consistent with designed bandwidth. Thus, the frequency responses of the two models are almost identical.

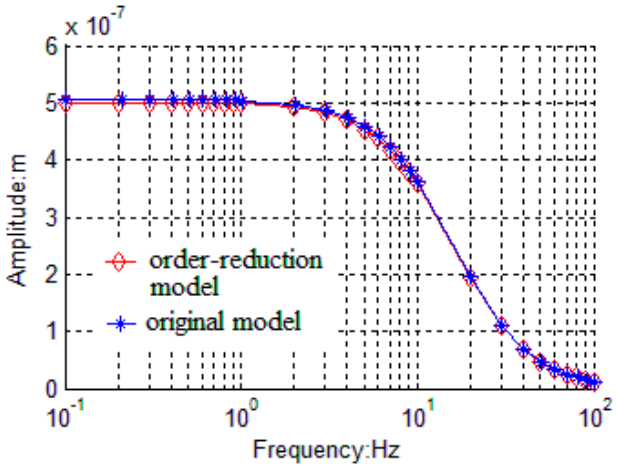

Figure 9. Frequency response characteristics of AGC loop based on the linearized model and the original model.

The experimental verification was conducted with a DRG test board. The designed PI controller of AGC loop is implemented in the ASIC. When the output frequency of NCO is fixed at the resonance frequency, the *C*/*V* output of primary mode which can represent displacement amplitude of primary mode, is tested using an oscilloscope, as shown in Figure 10. The rise time of the amplitude is 68 ms. The error of rise time between the experiment and model is about 13%, which is acceptable. Therefore, the experiment verified the validation of the linearization method of the AGC loop.

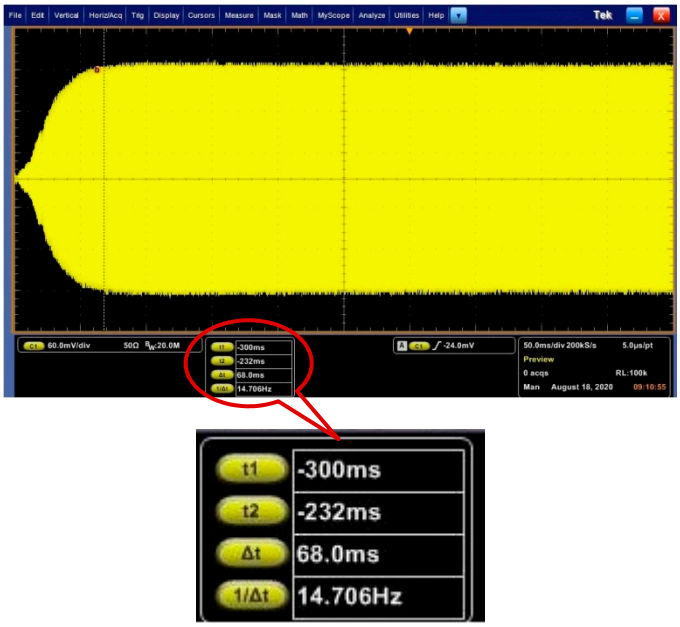

Figure 10. Start-up waveform of AGC loop with DRG experimental board.

According to the frequency responses and the step responses of the two models, it can be concluded that the linearized model is interchangeable with the original model. Therefore, closed-loop performance analysis and closed-loop controller design can be performed based on the linearized model.

3.2. PLL Model Linearizing and Closed-Loop Design

The PLL model mainly contains a digital phase detector, a PI controller, and a NCO. The NCO formed by a DDS (Direct Digital frequency Synthesizer) generates a sinusoidal or cosine signal. At the input of the NCO, an initial frequency ω_{int}, which is close to the resonant frequency, is generally added to reduce the time of the phase-lock and improve the efficiency of the phase-locked loop. The equivalent gain method is first used to simplify the PLL to the loop structure shown in Figure 11. At time t, it is assumed that the frequency of point F is ω_D and the output of the NCO at point G is $Y_G(t) = \cos(\omega_D t)$. Then, the signal at point H is $Y_H(t) = K_3 \cos(\omega_D t)$; here, $K_3 = k_{\text{drive}} \times k_{V2F}$.

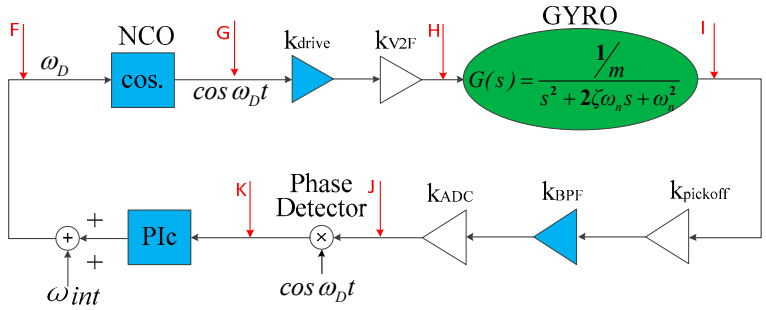

Figure 11. PLL loop after using equivalent gain method.

According to the amplitude-frequency characteristics of the gyroscopic resonator, the signal that reaches point I through the gyroscopic resonator is

$$Y_I(t) = K_3 * A(\omega_D) \cos(\omega_D t + \theta) \tag{24}$$

where

$$A(\omega_D) = \frac{\frac{1}{m\omega_n^2}}{\sqrt{\left[1 - \left(\frac{\omega_D}{\omega_n}\right)^2\right]^2 + \left(2\zeta\frac{\omega_D}{\omega_n}\right)^2}} \text{ and} \tag{25}$$

$$\theta = p(\omega_D) = \arctan\left(\frac{-\frac{2\zeta\omega_D}{\omega_n}}{1 - \left(\frac{\omega_D}{\omega_n}\right)^2}\right). \tag{26}$$

The input of the phase detector is set to $\Delta\omega$ ($\Delta\omega = \omega_n - \omega_D$); then, θ can be expressed by

$$\theta = p(\Delta\omega) = \arctan\left(\frac{\omega_n(\omega_n - \Delta\omega)}{(2\omega_n - \Delta\omega)\Delta\omega}\right). \tag{27}$$

The signal at point J is

$$Y_J(t) = K_3K_4 \times A(\omega_D) \cos(\omega_D t + \theta), \tag{28}$$

where $K_4 = k_{pickoff} \times k_{BPF} \times k_{ADC}$.

The signal reaching point K is

$$\begin{aligned} Y_K(t) &= K_3K_4A(\omega_D) \cos(\omega_D t + \theta) \times \cos(\omega_D t) \\ &= K_3K_4A(\omega_D)[\cos(2\omega_D t + \theta) + \cos\theta] \end{aligned} \tag{29}$$

As the phase detector has a low-pass filter function, the signal component at the frequency of $2\omega_D$ is filtered out. Therefore, the signal at point K is

$$Y_K(t) = K_3K_4A(\omega_D) \cos\theta. \tag{30}$$

Thus, the PLL shown in Figure 11 can be further derived to the loop shown in Figure 12.

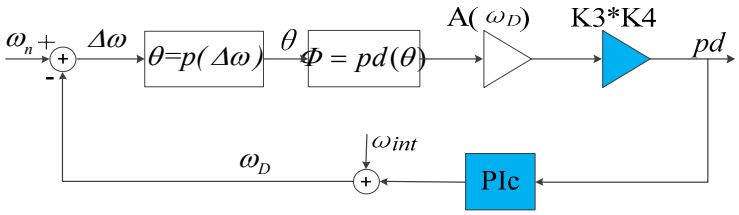

Figure 12. Order-reduction model of PLL.

In the loop shown in Figure 12, $\theta = p(\Delta\omega)$ and $\Phi = \cos(\theta)$ are both nonlinear modules. It is not convenient to design the closed-loop controller with automatic control theory; therefore, it is necessary to approximate the two modules to obtain a linear system.

According to Equations (27) and (30), the relationship between Φ and $\Delta\omega$ is plotted as shown in Figure 13. The slope of the curve in Figure 13 represents the gain from $\Delta\omega$ to Φ; however, the slope varies with $\Delta\omega$. When PLL is stable, $\Delta\omega = 0$; thus, the slope at $\Delta\omega = 0$ is used as the gain from $\Delta\omega$ to Φ while designing the loop controller.

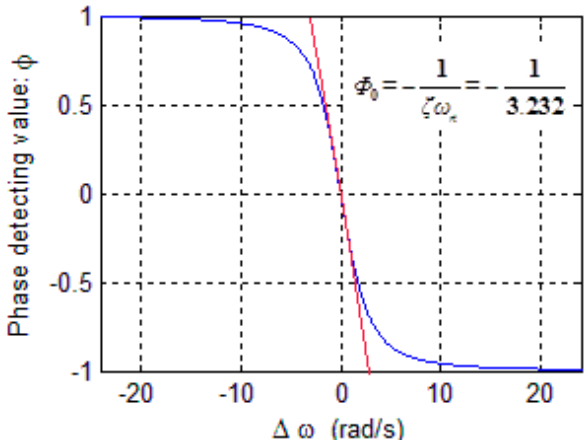

Figure 13. Relationship curve between Φ and $\Delta\omega$.

When the frequency of the drive signal ω_D approaches the gyroscopic resonant frequency ω_n, $A(\omega_D) \approx \frac{1}{2\zeta m\omega_n^2} = \frac{Q}{k}$ and $\theta \approx 90°$. When $\Delta\omega \to 0$, the slope of the curve is expressed by

$$\Phi_0 = \frac{d\Phi}{d(\Delta\omega)}|_{\Delta\omega\to 0} = -\frac{1}{\zeta\omega_n}. \quad (31)$$

Thus, when the PLL is stable, that is $\Delta\omega \to 0$, the modules <oscillator–gyroscope–phase detector> in series in PLL can be equivalent to a gain term:

$$pd(\Delta\omega) = -\frac{1}{\zeta\omega_n} \times A(\omega_n). \quad (32)$$

Here, the gain term in Equation (32) could be considered as the equivalent gain when ω_D does not equal to ω_n. Therefore, the models <oscillator–gyroscope–phase detector> in series can be approximated as a gain term as shown in Figure 14 when designing the closed-loop controller. The PLL can be linearized as shown in Figure 15.

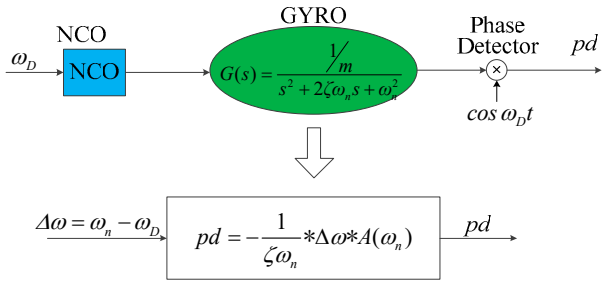

Figure 14. The models < oscillator–gyroscope–phase detector > in series are approximated as a gain term.

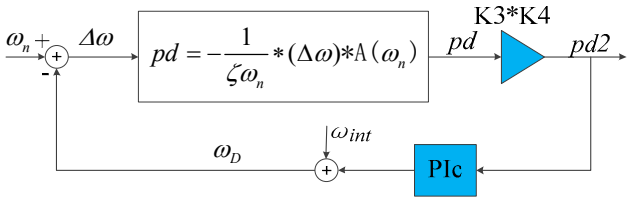

Figure 15. Linearized PLL.

The closed-loop controller is designed based on the linearized PLL loop. The PI controller is determined as $PI_{PLL}(s)=\frac{b}{s(s+a)}$; then, the closed-loop transfer function of linearized PLL is

$$\begin{aligned} C_{PLL}(s) &= \frac{\omega_{nc}^2}{s^2+2\zeta_c\omega_{nc}s+\omega_{nc}^2} \\ &= \frac{K_1K_2A(\omega_D)\Phi_0\times b}{s^2+as+K_1K_2A(\omega_D)\Phi_0\times b} \end{aligned} \tag{33}$$

Here, $2\zeta_c\omega_{nc}=a$ and $\omega_{nc}=\sqrt{K_1K_2A(\omega_D)\Phi_0\times b}$.

According to the configuring of ASIC and parameters of DRG, $K_3=3.44\times10^{-7}$, $K_4=3.78\times10^{11}$, and $A(\omega_D)=1.108$.

The systematic damping ratio of PLL ζ_c is designed to be 6 and for over-damping systems, the rise time (90% of the maximum value) is expressed by [31] $Tr=\frac{1+1.5\zeta_c+\zeta_c{}^2}{\omega_{nc}}$. The rise time is designed as 0.2 s, so $\omega_{nc}\approx300$. According to Equation (33), the PI controller of PLL is:

$$PI_{PLL}(s)=\frac{0.021}{s(s+3600)}. \tag{34}$$

The initial frequency ω_{int} is set to $\omega_{\text{int}}=12340*2\pi$ and the PI controller is introduced to the linearized model and the original model, respectively. The step response curves of the two models are shown in Figure 16a,b, respectively. According to Figure 16, the step response of the linear PLL model differs a little from the original model.

The rise time of the original model is 0.28 s while the rise time of the ideal model is 0.2 s. The rise time of the original model is longer than that of the linear model. This is because the equivalent gain term in linearized PLL is an approximation. Actually, the gain in the original PLL model is time-varying and is smaller than the equivalent gain term in linearized PLL when the PLL system is unstable. Therefore, the rise time of original PLL model is longer than that of the linear model, the linear PLL model is not completely maintained with the original model in the quantitative design. However, it is still of great significance for the qualitative analysis for the original model.

The experimental verification of PLL loop is also conducted with the designed PI controller. As the frequency cannot be directly reflected, and for PLL loop, only when the frequency is stable, the amplitude is stable, we consider the stable time of amplitude as the frequency stable time. We tested the start-up amplitude of primary mode when the AGC loop does not work. The waveform is shown

in Figure 17. The stable time of PLL loop is 295 ms which is close to the rise time of original model, and the error is about 5%.

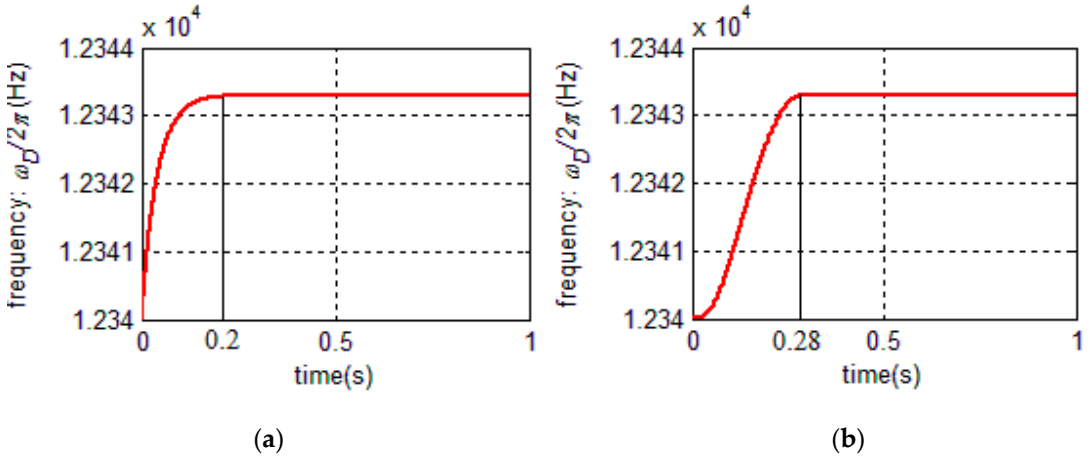

(**a**) (**b**)

Figure 16. (**a**) Step response of the PLL linearized model and (**b**) step response of the PLL original model.

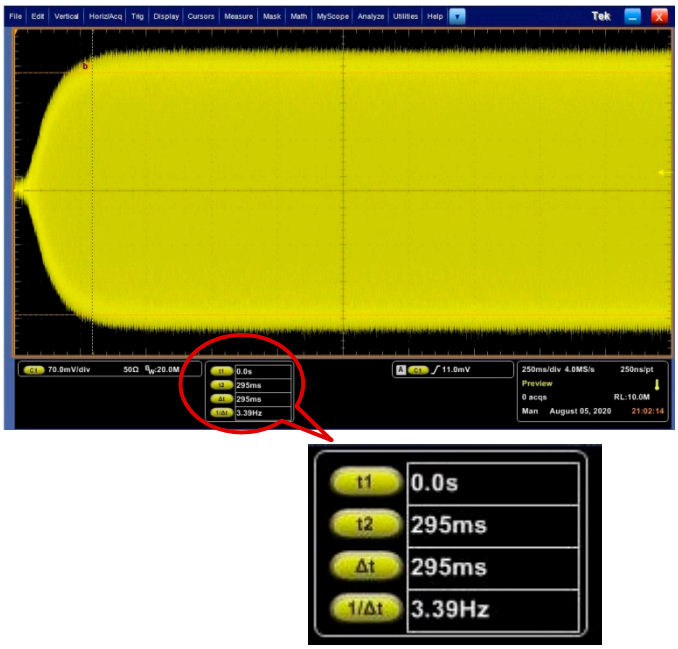

Figure 17. Start-up waveform of PLL loop with DRG experimental board.

So far, the gyroscopic model with a modulator and a demodulator in AGC loop is linearized to a first-order model, and the gyroscopic model with an oscillator and a phase detector in PLL is also linearized to a gain term. The PI controllers of the two loops are both designed using classical automatic control theory based on linearized models. The designed PI controllers are introduced to the original model as well as DRG experimental board, and it is verified that the method to linearize the gyroscopic model is useful.

4. Model Linearizing and Performance Analysis of Rebalance Loop

4.1. Model Order-Reduction and Closed-Loop Design of Rebalance Loop

The secondary mode includes a rebalance loop and a quardrate loop. As the basic principles and models of the two loops are almost the same and the rebalance loop determines many main performance terms of gyroscope, the rebalance loop is mainly analyzed.

The rebalance loop in the original model is shown in Figure 18a. The equivalent gain method is used to simplify the rebalance loop to the loop structure as shown in Figure 18b.

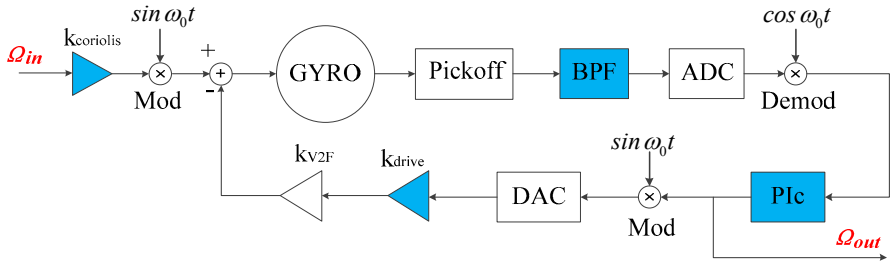

(**a**) Original model of the rebalance loop.

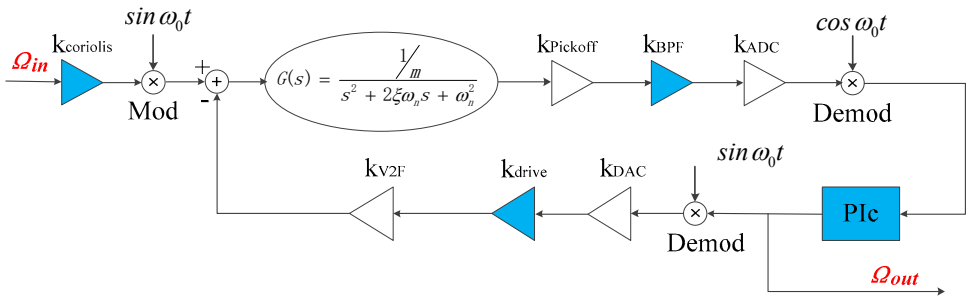

(**b**) Rebalance loop after using equivalent gain method.

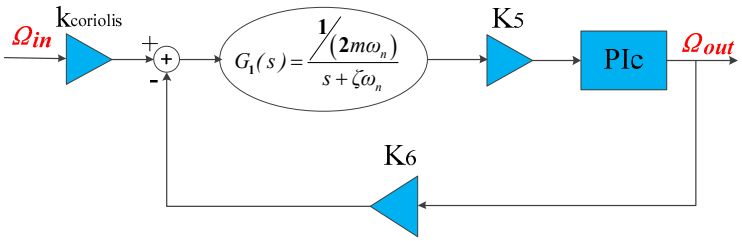

(**c**) Linearized model of rebalance loop.

Figure 18. Linearization process of the rebalance loop.

According to the conclusion in Section 3.1, the rebalance loop is order-reduced to a simplified loop as shown in Figure 18c. The terms K_5 and K_6 in Figure 18c are:

$$K_5 = k_{CV} \times k_{pickoff} \times k_{BPF} \times k_{ADC}, \text{ and} \tag{35}$$

$$K_6 = k_{V2F} \times k_{\mathrm{drive}} \times k_{DAC} \sqrt{2}. \tag{36}$$

The closed-loop transfer function of the rebalance loop is

$$C_{RB}(s) = k_{coriolis} \times \frac{K_5 \times PI(s) \times G_1(s)}{K_5 \times K_6 \times PI(s) \times G_1(s) + 1}. \tag{37}$$

The PI controller of the rebalance loop is determined by $PI(s) = \frac{b(s+\zeta\omega_n)}{s(s+a)}$; then, the closed-loop transfer function turns to

$$\begin{aligned} C_{RB}(s) &= k_{coriolis} \times \frac{\frac{\omega_{nc}^2}{K_6}}{s^2+2\zeta_c\omega_{nc}s+\omega_{nc}^2} \\ &= k_{coriolis} \times \frac{K_5 \times \frac{b}{m\omega_n}}{s^2+as+K_5 \times K_6 \times \frac{b}{m\omega_n}} \end{aligned} \tag{38}$$

where the terms ζ_c and ω_{nc} are the systematic damping ratio and resonant frequency of $C_{RB}(s)$, respectively, and $2\zeta_c\omega_{nc} = a$, $\omega_{nc} = \sqrt{K_5 \times K_6 \times \frac{b}{m\omega_n}}$.

4.2. Bandwidth Analysis

According to the closed-loop transfer function shown in Equation (38), the bandwidth can be designed by configuring the terms ζ_c and ω_{nc}. If ζc is set to 1, then the bandwidth Bw is $Bw = 0.64\omega_{nc}$.

Here, the bandwidth is desired to 50 Hz, then $\omega_{nc} = 490$. The terms K_5 and K_6 are calculated as $K_5 = 1.64 \times 10^{14}$ and $K_6 = 1.36 \times 10^{-11}$. Then the parameters of PI controller a and b are $a = 980$ and $b = 27.95$. Therefore, the closed-loop transfer function of the rebalance loop is

$$C_{RB}(s) = \frac{1.797 \times 10^9}{s^2 + 980s + 2.401 \times 10^5}. \tag{39}$$

The Bode diagram of the closed-loop transfer function, which represents the frequency response of linearized model, is shown in Figure 19.

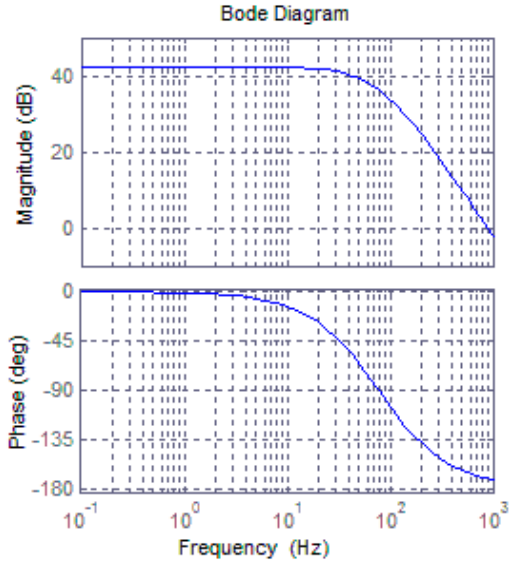

Figure 19. Bode diagram of the rebalance loop's linearized model.

The frequency response of the original rebalance loop is simulated with the designed PI controller as shown in Figure 20 and the amplitude–frequency characteristic curve shows accordance with that of the linearized model. Therefore, the bandwidth design based on the linearized model is effective for the original model.

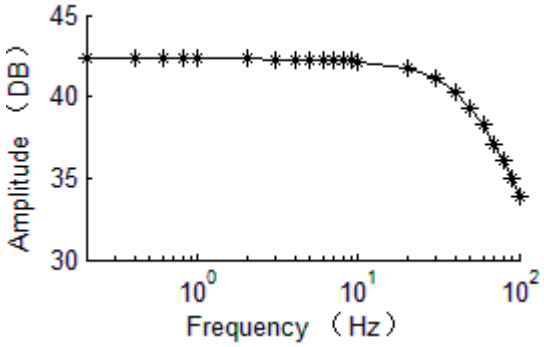

Figure 20. Amplitude–frequency characteristic curve of the original model.

The bandwidth of the DRG test system was carried out. The test result is shown in Figure 21. The tested bandwidth is 45 Hz. Compared with the designed bandwidth of the linear model, the error is 11%, which is acceptable. The experiment illustrates that the PI controller based on linear model is suitable for the real gyroscopic system.

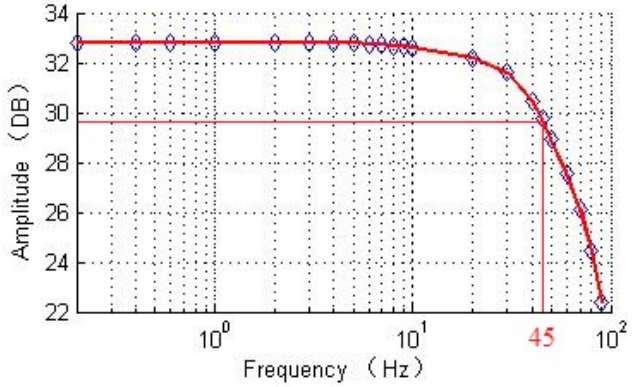

Figure 21. Tested bandwidth of DRG experimental board.

5. Discussion

In this paper, a closed-loop mechatronics model of a MEMS DRG with a configurable ASIC was established. The mechatronics model was linearized by the proposed order-reduction method (ORM). The controllers of all loops were designed using classical automatic control theory based on the linearized mechatronics. The linearized model was proved to show good agreement with the original mechatronics models in terms of system response. Meanwhile, the experimental verification was also carried out to demonstrate the validation of the method.

Any complex system needs to be reduced to an ideal system in order to use theoretical knowledge for analysis. Our work has built a bridge between the original mechatronics model and an ideal model. With the ideal model, the closed-loop system controller can be easily designed using classical automatic control theory and the systematical factors such as start-up time and bandwidth can be mathematically analyzed, which could hardly be done with the original mechatronics model. Depending on these analyses and mathematical conclusion, it is also helpful to guide the design of gyroscope resonator as well as circuit.

Author Contributions: Conceptualization, H.W. and J.X.; methodology, H.W., X.W., and J.X.; software, H.W.; validation, H.W., and X.W.; formal analysis, H.W.; investigation, H.W.; resources, J.X.; data curation, H.W., and X.W.; writing—original draft preparation, H.W.; writing—review and editing, X.W. and J.X.; project administration, J.X.; funding acquisition, J.X. All authors have read and agreed to the published version of the manuscript.

Funding: This work was supported by the Chinese National Science Foundation (grant no. 51775447) and National Key Research and Development Program of China, No. 2018YFB2002602.

Acknowledgments: The authors would like to thank Boyuan Zhou, Hongyu Chai, Keliang Wang, Jun Wu, Jinqiu Zhou, Zegang Ye, Miaomiao Kang, and Hong Zhu of Beijing Microelectronics Technology Institute (BMTI) for their support.

Conflicts of Interest: The authors declare no conflict of interest.

References

1. Challoner, A.D.; Ge, H.H.; Liu, J.Y. Boeing disc resonator gyroscope. In Proceedings of the 2014 IEEE/ION Position, Location and Navigation Symposium—PLANS 2014, Monterey, CA, USA, 5–8 May 2014; pp. 504–514.
2. Shcheglov, K.V.; Dorian Challoner, A. Isolated Planar Gyroscope with Internal Radial Sensing and Actuation. U.S. Patent No. 7040163, 9 May 2006.
3. Kubena, R.L.; David, T.C. Disc Resonator Gyroscopes. U.S. Patent No. 7581443, 1 September 2009.
4. Dorian Challoner, A.; David, W. Disc Resonator Integral Inertial Measurement Unit. U.S. Patent No. 7836765, 23 November 2010.
5. Senkal, D.; Askari, S.; Ahamed, M.J.; Ng, E.J.; Hong, V.; Yang, Y.; Ahn, C.H.; Kenny, T.W.; Shkel, A.M. 100K Q-factor toroidal ring gyroscope implemented in wafer-level epitaxial silicon encapsulation process. In Proceedings of the 2014 IEEE 27th International Conference on Micro Electro Mechanical Systems (MEMS), San Francisco, CA, USA, 26–30 January 2014.

6. Gerrard, D.D.; Ahn, C.H.; Flader, I.B.; Chen, Y.; Ng, E.J.; Yang, Y.; Kenny, T.W. Q-factor optimization in disk resonator gyroscopes via geometric parameterization. In Proceedings of the 2016 IEEE 29th International Conference on Micro Electro Mechanical Systems (MEMS), Shanghai, China, 24–28 January 2016.
7. Zhou, X.; Xiao, D.; Hou, Z.; Li, Q.; Wu, Y.; Yu, D.; Li, W.; Wu, X. Thermoelastic quality-factor enhanced disk resonator gyroscope. In Proceedings of the 2017 IEEE 30th International Conference on Micro Electro Mechanical Systems (MEMS), Las Vegas, NV, USA, 22–26 January 2017.
8. Zhou, X.; Xiao, D.; Li, Q.; Hou, Z.; He, K.; Chen, Z.; Wu, Y.; Wu, X. Decaying Time Constant Enhanced MEMS Disk Resonator for High Precision Gyroscopic Application. *IEEE/ASME Trans. Mech.* **2016**, *23*, 452–458. [CrossRef]
9. Ahn, C.H.; Ng, E.J.; Hong, V.A.; Yang, Y.; Lee, B.J.; Flader, I.; Kenny, T.W. Mode-Matching of Wineglass Mode Disk Resonator Gyroscope in (100) Single Crystal Silicon. *J. Mciroelectromech. Syst.* **2015**, *24*, 343–350. [CrossRef]
10. Lader, I.B.; Ahn, C.H.; Ng, E.J.; Yang, Y.; Hong, V.A.; Kenny, T.W. Stochastic method for disk resonating gyroscope mode matching and quadrature nulling. In Proceedings of the 2016 IEEE 29th International Conference on Micro Electro Mechanical Systems (MEMS), Shanghai, China, 24–28 January 2016.
11. Xiao, D.; Yu, D.; Zhou, X.; Hou, Z.; He, H.; Wu, X. Frequency Tuning of a Disk Resonator Gyroscope via Stiffness Perturbation. *IEEE Sens. J.* **2017**, *17*, 4725–4734. [CrossRef]
12. Xiao, D.; Zhou, X.; Li, Q.; Hou, Z.; Xi, X.; Wu, Y.; Wu, X. Design of a Disk Resonator Gyroscope With High Mechanical Sensitivity by Optimizing the Ring Thickness Distribution. *J. Microelectromech. Syst.* **2016**, *25*, 606–616. [CrossRef]
13. Zhou, X.; Xiao, D.; Hou, Z.; Li, Q.; Wu, Y.; Wu, X. Influences of the Structure Parameters on Sensitivity and Brownian Noise of the Disk Resonator Gyroscope. *J. Microelectromech. Syst.* **2017**, *26*, 519–527. [CrossRef]
14. HyuckAhn, C.; Shin, D.D.; Hong, V.A.; Yang, Y.; Ng, E.J.; Chen, Y.; Flader, I.B.; Kenny, T.W. Encapsulated disk resonator gyroscope with differential internal electrodes. In Proceedings of the 2016 IEEE 29th International Conference on Micro Electro Mechanical Systems (MEMS), Shanghai, China, 24–28 January 2016.
15. Shen, Q.; Chang, H.; Wu, Y.; Xie, J. Turn-on bias behavior prediction for micromachined Coriolis vibratory gyroscopes. *Measuremernt* **2019**, *131*, 380–393. [CrossRef]
16. Chorsi, H.T.; Chorsi, M.T.; Gedney, S.D. A Conceptual Study of Microelectromechanical Disk Resonators. *IEEE J. Multiscale Multiphysics Comput. Tech.* **2017**, *2*, 29–37. [CrossRef]
17. Chorsi, M.T.; Chorsi, H.T. Systematic analysis of carbon-based microdisk resonators. *FlatChem* **2020**, *20*, 100159. [CrossRef]
18. Chorsi, M.T.; Chorsi, H.T. Modeling and analysis of MEMS disk resonators. *Microsyst. Technol.* **2018**, *24*, 2517–2528. [CrossRef]
19. Chorsi, M.T.; Chorsi, H.T.; Gedney, S.D. Radial-contour mode microring resonators: Nonlinear dynamics. *Int. J. Mech. Sci.* **2017**, *130*, 258–266. [CrossRef]
20. Ahn, C.; Hong, V.; Park, W.; Yang, Y.; Chen, Y.; Ng, E.; Huynh, J.; Challoner, A.; Goodson, K.; Kenny, T. On-chip ovenization of encapsulated Disk Resonator Gyroscope (DRG). In Proceedings of the 2015 Transducers—2015 18th International Conference on Solid-State Sensors, Actuators and Microsystems (TRANSDUCERS), Anchorage, AK, USA, 21–25 June 2015.
21. Dion, F.; Martel, S.; DeNatale, J. 200mm High Performance Inertial Sensor Manufacturing Process. In Proceedings of the 2018 IEEE International Symposium on Inertial Sensors and Systems (INERTIAL), Moltrasio, Italy, 26–29 March 2018.
22. Sung, W.-T.; Sung, S.; Lee, J.G.; Kang, T. Design and performance test of a MEMS vibratory gyroscope with a novel AGC force rebalance control. *J. Micromech. Microeng.* **2007**, *17*, 1939–1948. [CrossRef]
23. Cui, J.; Chi, X.Z.; Ding, H.T.; Lin, L.T.; Yang, Z.C.; Yan, G.Z. Transient response and stability of the AGC-PI closed-loop controlled MEMS vibratory gyroscopes. *J. Micromech. Microeng.* **2009**, *19*, 1–17. [CrossRef]
24. Kraft, M.; Wilcock, R.; Almutairi, B. Innovative control systems for MEMS inertial sensors. In Proceedings of the 2012 IEEE International Frequency Control Symposium Proceedings, Baltimore, MD, USA, 21–24 May 2012.
25. Chen, F.; Yuan, W.; Chang, H.; Yuan, G.; Xie, J.; Kraft, M. Design and Implementation of an Optimized Double Closed-Loop Control System for MEMS Vibratory Gyroscope. *IEEE Sens. J.* **2013**, *14*, 184–196. [CrossRef]

26. Keymeulen, D.; Peay, C.; Foor, D.; Trung, T.; Bakhshi, A.; Withington, P.; Yee, K.; Terrile, R. Control of MEMS Disc Resonance Gyroscope (DRG) using a FPGA Platform. In Proceedings of the 2008 IEEE Aerospace Conference, Big Sky, MT, USA, 1–8 March 2008.
27. Polunin, P.M.; Shaw, S.W. Self-induced parametric amplification in ring resonating gyroscopes. *Int. J. Nonlin. Mech.* **2017**, *94*, 300–308.
28. Wang, H.; Ye, Z.; Zhang, Q.; Quan, H. System modeling, simulation and parameter analysis of MEMS vibrating ring gyroscope. *Navig. Control* **2017**, *16*, 25–32.
29. Sharma, M.; Kannan, A.; Cretu, E. Noise-based optimization and noise analysis for resonant MEMS structures. In Proceedings of the 2008 Symposium on Design, Test, Integration and Packaging of MEMS/MOEMS, Nice, France, 9–11 April 2008.
30. Putty, M. A micromachined vibrating ring gyroscope. Ph.D. Thesis, University of Michigan, Ann Arbor, MI, USA, 1995.
31. Zhang, A. *Automatic Control Theory*, 1st ed.; Tsinghua University Press: Beijing, China, 2006; pp. 154–196.